Three-Dimensional β-Amyloid Burden Correlation Between the Eye and Brain in Alzheimer's Disease Mice Using Light-Sheet Fluorescence Microscopy

Hye Joo Son,[1] Seonok Kim,[2] Seog-Young Kim,[3,4] Jin Hwa Jung,[4] Suk Hyun Lee,[5] Soo-Jong Kim,[6] Chanwoo Kim,[7] and Alice Hahn[8]

[1]Department of Nuclear Medicine, Dankook University Medical Center, Dankook University College of Medicine, Cheonan, Chungnam, Republic of Korea
[2]Department of Clinical Epidemiology and Biostatistics, Asan Medical Center, University of Ulsan College of Medicine, Seoul, Republic of Korea
[3]Department of Convergence Medicine, University of Ulsan College of Medicine, Seoul, Republic of Korea
[4]Convergence Medicine Research Center, Asan Medical Center, Seoul, Republic of Korea
[5]Department of Radiology, Hallym University Kangnam Sacred Heart Hospital, Hallym University College of Medicine, Seoul, Republic of Korea
[6]Mallinckrodt Institute of Radiology, Washington University School of Medicine in St. Louis, Saint Louis, Missouri, United States
[7]Department of Nuclear Medicine, Kyung Hee University Hospital at Gangdong, College of Medicine, Kyung Hee University, Republic of Korea
[8]Department of Mental Health, Johns Hopkins Bloomberg School of Public Health, Baltimore, Maryland, United States

Correspondence: Hye Joo Son, Department of Nuclear Medicine, Dankook University Medical Center, Dankook University College of Medicine, Cheonan 31116, Republic of Korea; neuroscience@dankook.ac.kr.

Received: September 21, 2024
Accepted: February 17, 2025
Published: March 18, 2025

Citation: Son HJ, Kim S, Kim SY, et al. Three-dimensional β-amyloid burden correlation between the eye and brain in alzheimer's disease mice using light-sheet fluorescence microscopy. *Invest Ophthalmol Vis Sci.* 2025;66(3):34. https://doi.org/10.1167/iovs.66.3.34

Purpose. Recent studies have highlighted the significance of peripheral β-amyloid (Aβ) deposition, identifying the eye as a potential early detection site for Alzheimer's disease (AD). However, previous two-dimensional AD ocular studies have been unable to establish a clear correlation between the three-dimensional Aβ accumulation in the entire eyeball and brain while preserving structural integrity. This study employed a combined brain amyloid positron emission tomography/magnetic resonance (PET/MR) and light-sheet fluorescence microscopy (LSFM) platform to assess whether the three-dimensionally measured Aβ burden in the eyeball correlates with that in the brain.

Methods. Thirteen eyeballs (6 AD, 7 control) and 17 brains (10 AD, 7 control) were collected from ten 44-week-old 5xFAD and seven control mice. The samples underwent tissue clearing and staining with thioflavin S (Aβ), anti-CD11b (microglia), and anti–ACSA-2 (astrocytes) for LSFM imaging and quantified via 3D surface volume. Standardized uptake value ratios from [^{18}F]Flutemetamol PET/MR were also calculated.

Results. AD eyeballs presented significantly greater plaque-like surface volumes (median, 51,091,002 μm^3 [interquartile range, 38,488,272–64,869,828]) than controls (229,293 μm^3 [115,863–311,5320]; $P = 0.001$). AD brains exhibited higher [^{18}F]Flutemetamol uptake and greater plaque-like surface volumes (898,634,368 μm^3 [556,263,488–1,105,326,720]) than controls (33,320,178 μm^3 [26,842,538–62,716,956]; $P < 0.001$). A strong positive correlation was observed between the plaque-like surface volumes in the brain and that in the eyeball ($r = 0.810$, $P = 0.001$). No significant correlations were found in other morphologic parameters.

Conclusions. Our observation of a strong correlation between the three-dimensional Aβ burden in the whole eyeball and brain advances our understanding of the systemic nature of Aβ pathology and suggests ocular Aβ as a potential independent predictor of brain Aβ burden.

Keywords: alzheimer's disease, amyloid, eye, light-sheet microscope, tissue clearing

With the accelerated development of Alzheimer's disease (AD) therapies, exemplified by the phase III trial of lecanemab,[1,2] a growing focus on establishing disease-specific screening biomarkers for early diagnosis in the preclinical stage (pathology positive, clinical negative) has been noted, aiming for secondary prevention by reducing early-stage AD pathology accumulation and delaying symptom onset. Recently, the focus of AD research has undergone a paradigmatic shift, extending beyond the traditional confines of central nervous system (CNS) pathology. The eye, an extension of the CNS with a shared embryologic origin and structural, functional, and immunologic

systems, presents an opportunity for the noninvasive assessment of neural integrity.[3] retinal ganglion cell axons forming the optic nerve extend to the lateral geniculate nucleus and the superior colliculus, facilitating the transport of amyloid precursor protein (APP) produced by retinal ganglion cells.[3]

In several neurodegenerative disorders, ocular manifestations precede conventional CNS-based diagnoses.[3] Patients with AD exhibit visual manifestations, including decreased visual acuity, contrast sensitivity, and poor color discrimination.[4] Current advances in noninvasive, high-resolution ophthalmologic technologies such as optical coherence tomography (OCT) and blue-light autofluorescence have significantly enhanced the early detection of subtle neuropathologic changes in the eyes of patients with preclinical AD.[3] Ocular AD biomarkers are recognized as cost-effective and widely acceptable screening tools for early dementia diagnosis, owing to their direct accessibility.

Although ocular amyloid-beta (Aβ) deposition has been reported in several human and animal studies,[5–7] no previous studies have established a correlation between the quantitative parameters for three-dimensional (3D) Aβ accumulation in the whole intact eyeball and the whole-brain Aβ load. In a previous study analyzing human Aβ (hAβ) expression in homogenate fractions of lenses and brain from Tg2576 mice by anti-hAβ immunoblot and enzyme-linked immunosorbent assay (ELISA), the average total hAβ concentration increased with age in both tissues.[8] In another study of APPswe/PS1dE9 transgenic mice, ELISA measurements revealed a significant correlation between Aβ levels in the retina and cerebrum ($r = 0.7291$, $P = 0.0014$), although curcumin's inhibitory effect on Aβ attenuated this association.[9] However, these earlier studies focused predominantly on the retina and posterior regions of the eye, hindering a comprehensive assessment of the entire eyeball, and relied on traditional experimental techniques[5–7] that involved homogenized samples or thin, two-dimensional (2D) sections of localized subregions. Such approaches disrupt the intrinsic spherical structure of the whole eyeball and limit the ability to comprehensively assess the 3D spatial distribution of Aβ particles within intact ocular structures. Given the diverse 3D morphologic profiles of Aβ—each playing distinct roles in neurotoxicity and disease progression—quantification based on 2D sections fails to accurately reflect these 3D Aβ features. Light-sheet fluorescence microscope (LSFM), combined with tissue-clearing technologies, enables in-depth 3D visualization of neuropathologic networks within the fully transparent, whole eyeball—a level of detail previously unattainable with conventional techniques.[10]

In this study, we aimed to investigate the correlation between Aβ burden in the whole eyeball and the brain using an innovative platform that integrates amyloid brain positron emission tomography (PET)/magnetic resonance (MR) and LSFM. Specifically, we focused on the 3D spatial distribution of AD-related pathology in the chemically cleared eyeballs and brains of 5xFAD transgenic AD mice to support our hypothesis that Aβ burden measured in the whole eyeball significantly correlates with that in the brain.

Methods

Animal

We assembled a cohort of ten 44-week-old female 5xFAD mice (Jackson Laboratory, Bar Harbor, ME, USA) and seven 31-week-old female C57BL/6J mice as controls. The choice of 31-week-old control mice was determined by practical considerations, including animal availability and the scheduling requirements for MR and PET imaging. The 5xFAD model overexpresses five familial AD mutations in human APP (the Swedish [K670N, M671L], Florida [I716V], and London [V7171]) and PSEN1 (M146L and L286V), driven by the neural-specific Thy1 promoter.[11] We selected the 44-week (approximately 11-month) time point for our cohort of female 5xFAD mice because the purpose of our study was to evaluate the correlation between Aβ burden in the whole eyeball and that in the brain, and sufficient accumulation of Aβ plaques in both tissues at this stage was essential to allow for a meaningful assessment of this correlation. By 2 months of age, the 5xFAD model exhibits extracellular Aβ formation in the subiculum and cortical layer V, which is accompanied by astrogliosis and microgliosis.[11] Widespread Aβ plaques and significant neuronal loss occur by 6 and 9 months, respectively.[11] In a previous study investigating the relationship between brain and retinal Aβ plaque deposition in 5xFAD mice at 6, 12, and $\geq$14 months of age, Aβ plaque loads increased significantly and sharply between 6 and 12 months of age in the retina, hippocampus, and cortex.[12] Another study examining age-related patterns of soluble and insoluble Aβ deposition and their impact on retinal structure and function in the 5xFAD mouse model reported that at 6 months of age, Aβ labeling was confined to the inner retinal layers, with no detectable immunoreactivity in the outer retina.[13] However, by 12 and 17 months, positive Aβ staining was observed in the ganglion cell layer, inner plexiform layer, outer plexiform layer, inner nuclear layer, and outer nuclear layer of the retina.[13] By 9 to 10 months, 5xFAD mice show well-established Aβ plaques and associated neuropathology in both the brain and retina. All mice were housed in temperature-controlled conditions (22 $\pm$ 2°C, 55% $\pm$ 10% humidity) with a 12-hour light/dark cycle. This study adhered to the ARVO Statement for the Use of Animals in Ophthalmic and Vision Research. All animal experiments were approved by the Dankook Institutional Animal Care and Use Committee (DKU-22-080).

Brain Amyloid PET/MRI Acquisition and Analysis

Brain [^{18}F]Flutemetamol PET/MR imaging (MRI) was performed using a nanoScan PET/MRI (1T; Mediso, Budapest, Hungary). The mice were anesthetized (1.5% isoflurane in 100% O_2 gas) and intravenously injected with [^{18}F]Flutemetamol (0.3–0.4 mCi) through the tail vein. PET static images were acquired for 20 minutes (20–40 minutes postinjection) and reconstructed in Tera-Tomo 3D using full detector mode. T1-weighted gradient-echo 3D sequences and T2-weighted fast spin-echo MR images were acquired for anatomic reference and attenuation correction. The 7T T2-weighted brain MR images were used for template generation of PET/MR images. For quantification, we used an in-house amyloid-specific mouse brain PET template for spatial normalization. We manually performed skull-stripping on the control mice using ITK-SNAP to create brain masks on individual T2 MR images.[14] These masks were then applied to the MRIs and spatially normalized to the mouse brain T2 template. The coregistered PET images were normalized to the template space using MRI normalization parameters, and a final template was generated by averaging and smoothing these normalized images. For both groups, spatial normalization was performed by cropping the whole-body PET scans

to preserve only the head region and to align the scans with the mouse brain PET template. These head-region images were first aligned to the in-house mouse brain PET template using rigid body registration and then spatially normalized to the template space. Finally, the mouse atlas in PMOD Biomedical Image Quantification and Kinetic Modeling Software (Version 4.3; PMOD Technologies LLC, Zurich, Switzerland) was used for region-of-interest (ROI)–based quantitative analysis of the spatially normalized PET images. We used standardized uptake value ratios (SUVRs) for the relative quantification of [^{18}F]Flutemetamol PET scans. The whole cerebellum served as the reference region for this quantification (detailed description in Supplementary Method).[15]

Hydrophilic Tissue Clearing and LSFM Imaging

After transcranial perfusion, extracted brains and eyeballs were fixed in 4% paraformaldehyde solution in PBS. The brains were then dissected into 1-mm sagittal sections targeting the CA1 hippocampal region, while the eyeballs remained intact. Tissue clearing was performed using the hydrophilic Binaree Tissue Clearing Kit (HRTI-012; Binaree, Daegu, Korea). After three 20-minute washes with 1× PBS at 4°C, samples were incubated in 10 mL of starting solution at 37°C for 48 hours, shaking at 50 rpm. The solution was then replaced with 10 mL of Tissue Clearing Solution A, and the samples were incubated at 42°C with shaking at 50 rpm for 2 days (48 hours) to achieve initial clearing. Following this, the clearing solution was removed, and the samples were transferred to a tube containing 5 mL of triple-distilled water (TDW) to perform a washing step. Since the clearing solution is highly viscous, the samples were carefully retrieved using forceps to avoid damage. The washing was conducted at 10°C with shaking at 50 rpm for 1 hour, and this process was repeated four times, with fresh TDW added for each wash. Despite careful handling, the repeated solution exchanges and mechanical stress during these steps may have further contributed to tissue damage, particularly in partially cleared eye globes. After completing the washing steps, the TDW was replaced with 3 mL of Tissue Clearing Solution B, and the samples were incubated at 42°C with shaking at 50 rpm for 2 days (48 hours). Finally, a 48-hour permeabilization step was performed at 37°C with shaking at 50 rpm using 3 mL of a solution containing 0.2% Triton X-100 and 10% dimethyl sulfoxide in 0.1× PBS to facilitate subsequent antibody penetration. Among the 17 eyeballs collected (1 eyeball per mouse: 10 AD and 7 control mice), 4 AD mouse eyeballs were damaged during the clearing process. Consequently, the final steps were conducted on 6 AD eyeballs, 7 control eyeballs, 10 AD brains, and 7 control brains. Subsequently, the samples were treated with thioflavin-S (488 nm, Aβ) at a concentration of 1×10^{-5}%, selected as optimal based on both published data[16] and preliminary testing over a range of 1% to 1×10^{-8}%. At the higher concentration (1%), plaques were readily visualized, but excessive background fluorescence obscured finer details; at 1×10^{-8}%, background fluorescence was negligible, but plaque visibility was diminished. By balancing plaque signal intensity against nonspecific fluorescence, we identified 1×10^{-5}% as providing "specific" staining through an optimal ratio of bright plaque labeling to minimal background fluorescence. The samples were then stained with anti-mouse ACSA-2 antibody (647 nm) for astrocytes and anti-mouse CD11b antibody (561 nm) for microglia.

High-resolution LSFM imaging of ex vivo brain and eyeball samples was performed using a Zeiss Lightsheet Z.1 microscope (Carl Zeiss Meditec, Oberkochen, Germany) with a 5× illumination lens (0.1 NA) and a 5× objective lens (EC Plan-Neofluar, 0.16 NA; Carl Zeiss AG, Oberkochen, Germany) at a 0.71× zoom factor. The system was calibrated for three excitation wavelengths: 647 nm for astrocytes, 555 nm for microglia, and 488 nm for Aβ detection. Single-illumination mode was used to enhance the signal-to-noise ratio and image clarity. The 3D surface models for each wavelength were generated using Imaris software (Version 7.2.3, Bitplane AG, Zurich, Switzerland). To designate a computational surface model of individual amyloid particle of interest, the Surface creation tool was used to generate a ROI. To ensure reproducibility and minimize user bias, we employed the automated thresholding functionalities integrated into the Imaris software, which algorithmically determined thresholds using standardized parameters without manual adjustments. The initial threshold was determined using Gaussian filtering, background subtraction, and auto-local thresholding, which standardized segmentation by enhancing the signal-to-noise ratio, reducing noise, and preserving structural integrity.[17–20] Surface smoothing was performed using a 4-µm grain size, corresponding to the smallest discernible cellular markers in slice-mode observations, to define amyloid particle borders.[18] Background subtraction (local contrast) in Imaris isolated foreground particles from the background by calculating a variable baseline intensity for each voxel and subtracting it from the original intensity.[18] Auto-local thresholding enhanced segmentation accuracy by dynamically adjusting intensity thresholds based on local image characteristics, with the Niblack method effectively handling uneven illumination and noise by calculating thresholds from the local mean and standard deviation.[21–24] While automated thresholding was the primary method, a subsequent manual correction step addressed errors such as misidentifying noncellular particles (e.g., fibrous dust), ensuring a refined semiautomated process that balanced accuracy and consistency. Furthermore, to minimize bias, all data were anonymized, and analysts performed thresholding and manual corrections while blinded to the animals' genotypes, PET results, and experimental conditions. Finally, volumetric data extraction of each particle was performed using the "Statistics" function in the "Surpass" tab of the Imaris interface, selecting the "Volume" metric from the available measurement parameters. Additionally, unique identifiers were assigned to individual particles using the "Object ID" feature, allowing calculation of each amyloid particle's surface area and volume, which were then summed to obtain the total surface area and volume. Statistical validation was performed by applying a 95% confidence interval to the voxel dimensions, accurately determining the volumetric characteristics of the surface models.

Statistics

Data are presented as the medians [interquartile range (IQR)]. The right-skewed variables (total surface volume [µm^3] of ocular amyloid, brain microglia, and astrocytes; total number of plaque-like features, total surface area [µm^2]; and individual surface area [µm^2] of ocular plaque-like features) were analyzed after log transformation. A *t*-test or Wilcoxon rank-sum test was used to assess differences in quantitative parameters between groups. After log

Investigative Ophthalmology & Visual Science

transformation, normality was assessed using the Shapiro–Wilk test. If normality was satisfied, comparisons were made using the *t*-test; otherwise, the Wilcoxon rank-sum test was applied. Pearson's or Spearman's correlation analyses were conducted to evaluate the correlation between various Aβ quantitative and morphologic parameters in the brain and the eyeball. A two-sided P value <0.05 was considered statistically significant. All the statistical analyses were performed using SAS version 9.4 (SAS Institute, Cary, NC, USA) and R 4.2.2 (https://cran.r-project.org/).

Results

Three-Dimensional Aβ Distribution in Eyes and Brains of 5xFAD Mice Via LSFM Imaging

Using advanced LSFM with tissue clearing, we investigated the 3D distribution of key neuropathological markers—thioflavin-S for Aβ, CD11b for microglia, and ACSA-2 for astrocytes—in the eyeballs and brains of AD and control mice. In the visual comparison, AD mice exhibited significantly greater accumulation of Aβ plaque-like features in the eyes compared to the controls. Within the eyeball, the accumulation of Aβ plaque-like features was predominantly distributed in the retina and optic nerve, as well as in the anterior regions, including the iris, limbus, and lens (Fig. 1, Supplementary Fig. S1, Supplementary Videos S1 and S2). Similarly, the brain tissues of AD mice showed more extensive deposition of Aβ plaque-like features compared to the controls (Fig. 2B, Supplementary Video S3).

Comparison of Quantitative and Morphologic Parameters of Ocular Aβ Plaque-Like Features Between AD and Control Groups

With respect to the total ocular amyloid load, the eyeballs of AD mice presented a significantly greater total number (AD: median, 7747 [IQR, 2612–9866]; control: 1286 [659–1680]; $P = 0.019$), total surface area (AD: 11,189,654 μm^2 [4,491,474–14,954,527]; control: 147,599 μm^2 [124,661–1,261,400]; $P = 0.003$), and total surface volume (AD: 51,091,002 μm^3 [38,488,272–64,869,828]; control: 229,293 μm^3 [115,863–3,115,320]; $P = 0.001$) of plaque-like feature accumulation than did those of control mice. Regarding individual particle size, the eyeballs of AD mice also presented significantly greater individual surface areas (AD: 1481 μm^2 [646–1720]; control: 186 μm^2 [161–648]; $P = 0.003$) and individual surface volumes (AD: 5900 μm^3 [1663–8995]; control: 261 μm^3 [190–1697]; $P = 0.001$) of plaque-like feature accumulation than the control mice. Assigning unique identi-

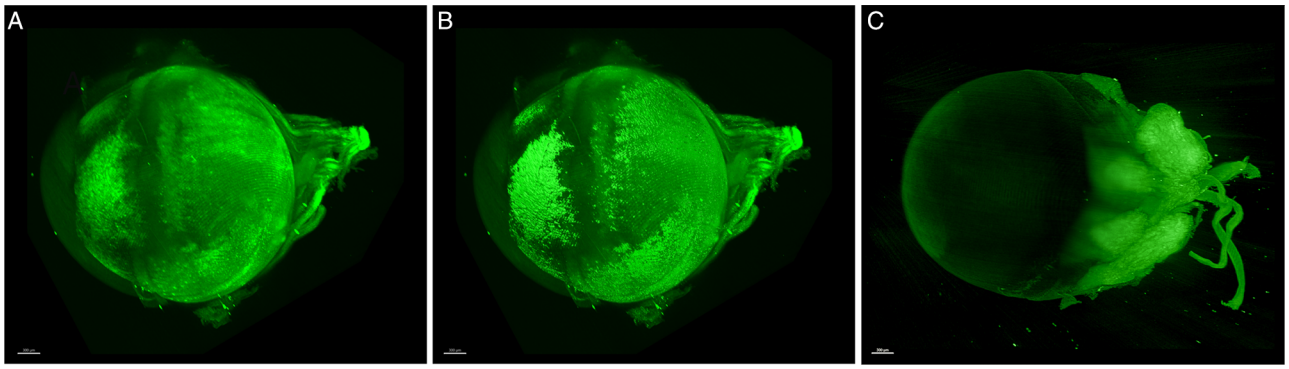

Figure 1. Light-sheet fluorescence images of β-amyloid in AD and control mouse eyeball. (**A**) Representative images of light-sheet fluorescence microscope imaging with hydrophilic tissue clearing and volume staining using thioflavin-S (488 nm, green channel) for β-amyloid in the eyeballs of 44-week-old 5xFAD mice. (**B**) Imaris-based volume rendering surface model for β-amyloid in the eyeballs of AD mice. (**C**) Representative images of light-sheet fluorescence microscope imaging with hydrophilic tissue clearing and volume staining using thioflavin-S (488 nm, green channel) for β-amyloid in the eyeballs of control mice.

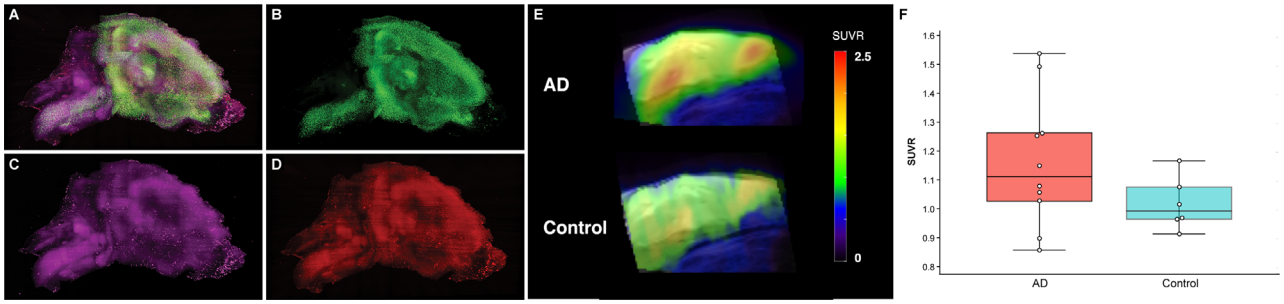

Figure 2. Evaluation of brain β-amyloid accumulation using both light-sheet fluorescence microscopy and [^{18}F]Flutemetamol PET/MR imaging. (**A**) Representative images of light-sheet fluorescence microscope imaging with hydrophilic tissue clearing and volume immunostaining of the brain of 44-week-old 5xFAD mice (merged image). (**B**) Green channel (488 nm) with volume staining for thioflavin-S, a specific marker for amyloid. (**C**) Purple channel (647 nm) with volume immunostaining with anti–ACSA-2, a specific marker for astrocytes. (**D**) Red channel (561 nm) with volume immunostaining with anti-CD11b, a specific marker for microglia. (**E**) Visual comparison [^{18}F]Flutemetamol brain PET/MR imaging in representative AD and control mice. Note: The color bar for SUVR ranges from 0 to 2.5. (**F**) Quantitative group comparison of cortical SUVR between the AD and control groups.

Investigative Ophthalmology & Visual Science

Table 1. Comparison of the Quantitative and Morphologic Parameters of Ocular and Brain Amyloid Between AD and Control Groups

Organ and Quantitative Parameter	AD, Median [IQR]	Control, Median [IQR]	*P* Value*
Eyeball			
Ocular amyloid total plaque number†	7747 [2612–9866]	1286 [659–1680]	0.019*
Ocular amyloid total plaque surface area (μm^2)†	11,189,654 [4,491,474–14,954,527]	147,599 [124,661–1,261,400]	0.003*
Ocular amyloid total surface volume (μm^3)†	51,091,002 [38,488,272–64,869,828]	229,293 [115,862–3,115,320]	0.001*
Ocular amyloid individual plaque area (μm^2)†	1481 [646–1720]	186 [161–648]	0.002*
Ocular amyloid individual plaque volume (μm^3)†	5900 [1663–8995]	261 [190–1697]	0.001*
Ocular amyloid ellipticity (oblate)†	0.18 [0.18–0.19]	0.17 [0.16–0.19]	0.708
Ocular amyloid ellipticity (prolate)†	0.75 [0.74–0.76]	0.77 [0.76–0.79]	0.643
Ocular amyloid sphericity‡	0.69 [0.67–0.69]	0.69 [0.68–0.69]	0.567
Brain			
Brain amyloid total plaque number†,§	58,326 [53,324–64,346]	175,241 [151,035–232,121]	<0.001*
Brain amyloid total plaque surface area (μm^2)†	179,019,864 [117,849,088–213,864,800]	33,627,468 [26,550,408–43,610,360]	<0.001*
Brain amyloid total surface volume (μm^3)†	898,634,368 [556,263,488–1,105,326,720]	33,320,178 [26,842,538–62,716,956]	<0.001*
Brain amyloid individual plaque area (μm^2)‡	3685 [3014–3755]	154 [136–237]	0.001*
Brain amyloid individual plaque volume (μm^3)‡	17,211 [12,682–17,828]	155 [124–327]	0.001*
Brain amyloid ellipticity (oblate)‡	0.31 [0.30–0.32]	0.14 [0.13–0.15]	0.001*
Brain amyloid ellipticity (prolate)‡	0.48 [0.47–0.50]	0.82 [0.81–0.84]	0.001*
Brain amyloid sphericity†,§	0.84 [0.83–0.85]	0.68 [0.67–0.69]	<0.001*
Brain amyloid PET SUVR†,§	1.12 [1.04–1.27]	1.00 [0.97–1.08]	0.167
Brain astrocyte total surface volume (μm^3)†,§	59,064,360 [39,531,352–108,245,992]	20,272,722 [12,365,537–26,177,505]	0.005*
Brain microglia total surface volume (μm^3)†,§	51,210,100 [41,950,104–56,498,836]	23,461,594 [17,099,503–27,573,731]	<0.001*

* $P < 0.05$ was considered statistically significant.
† *t*-test.
‡ Wilcoxon rank-sum test.
§ The right-skewed variables were analyzed after log transformation.

fiers to individual plaque-like particles within each mouse's eyeball facilitated the quantification of their volume (μm^3) and allowed 3D visualization of the total number and distribution of plaque-like features. This revealed significant intraindividual variability in the surface volume of individual plaque-like features within the same specimen and notable interindividual variability in both the total number of plaque-like features and the individual volume distribution among different samples within the same AD group (Fig. 4, Supplementary Video S4). Furthermore, there were no statistically significant differences in the morphologic shape parameters of individual plaque-like features, such as oblate/prolate ellipticity, prolate ellipticity, and sphericity (Table 1).

Comparison of [^{18}F]Flutemetamol PET/MR and LSFM Brain Aβ Imaging Parameters Between AD and Control

In the LSFM images, although the AD mice had significantly fewer total plaque-like numbers (AD: 58,326 [53,324–64,346]; control: 175,241 [151,035–232,121]; $P < 0.001$), their brains exhibited a significantly greater total surface area (AD: 179,019,864 μm^2 [117,849,088–213,864,800]; control: 33,627,468 μm^2 [26,550,408–43,610,360]; $P < 0.001$) and a significantly greater total surface volume (AD: 898,634,368 μm^3 [556,263,488–1,105,326,720]; control: 33,320,178 μm^3 [26,842,538–62,716,956]; $P < 0.001$) of plaque-like features compared to controls (Fig. 3B, Table 1). Individual plaque-like features in the brains of AD mice also showed significantly larger surface areas (AD: 3685 μm^2 [3014–3755]; control: 154 μm^2 [136–237]; $P = 0.001$) and surface volumes (AD: 17,211 μm^3 [12,682–17,828]; control: 155 μm^3 [124–327]; $P = 0.001$). Additionally, significant differences were found in morphologic shape parameters such as oblate ellipticity (AD: 0.31 [0.30–0.32]; control: 0.14 [0.13–0.15]; $P = 0.001$), prolate ellipticity (AD: 0.48 [0.47–0.50]; control: 0.82 [0.81–0.84]; $P = 0.001$), and sphericity (AD: 0.84 [0.83–0.85]; control: 0.68 [0.67–0.69]; $P < 0.001$) (Table 1). In [^{18}F]Flutemetamol brain PET/MR visual analysis, AD mice showed higher β-amyloid uptake than controls (Fig. 2E), although the cortical SUVR difference was not statistically significant (AD: 1.12 [1.04–1.27]; control: 1.00 [0.97–1.08]; $P = 0.167$) (Fig. 2F).

Correlation Between Aβ Plaque-Like Feature Quantitative and Morphologic Parameters in the Brain and Eyeball

Regarding total plaque-like feature load, we observed a strong positive correlation between total surface volume in the eyeball and that in the brain ($r = 0.810$, $P = 0.001$) (Fig. 5A, Table 2), and total surface area in the brain was also strongly correlated with that in the eyeball ($r = 0.722$, $P = 0.005$) (Fig. 5B, Table 2). At the level of individual plaque-like features, total surface volume ($r = 0.824$, $P = 0.001$) and surface area ($r = 0.808$, $P = 0.001$) in the brain correlated with those in the eyeball (Figs. 5C, 5D, Table 2). However, there were no significant correlations between morphologic shape parameters, such as ellipticity or sphericity, in the brain and eyeball (Table 2). Additionally, there was no significant correlation between total surface volume in the eyeball and brain [^{18}F]Flutemetamol PET/MR cortex SUVR ($r = 0.399$, $P = 0.199$) (Table 2).

Increased Astrocyte and Microglial Expression in AD Mouse Brains but Not in Eyeballs

In AD brains, neuroinflammation was marked by higher expression of CD11b in microglia (AD: 51,210,100 μm^3 vs. control: 23,461,594 μm^3; $P < 0.001$) and ACSA-2 in astrocytes (AD: 59,064,360 μm^3 vs. control: 20,272,722 μm^3; $P = 0.005$) compared to controls (Figs. 2C, 2D, Table 1).

Investigative Ophthalmology & Visual Science

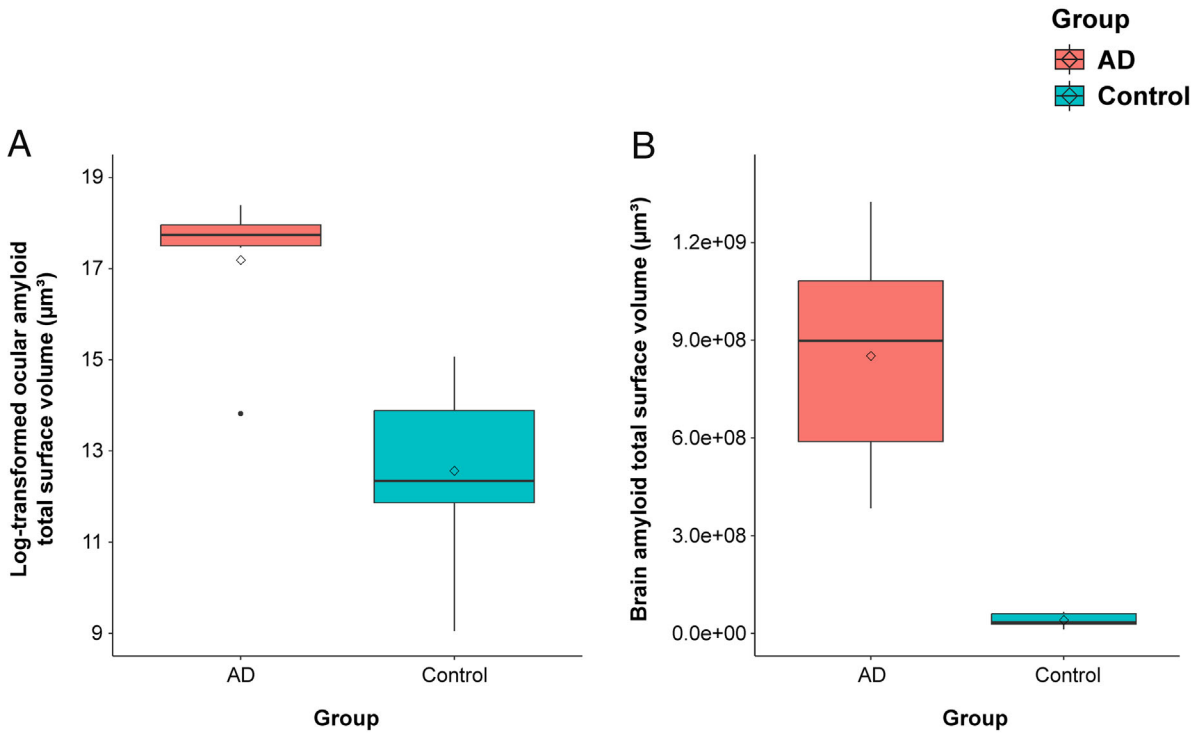

Figure 3. Comparison of total amyloid load in the eyeball and brain between AD and control groups. (**A**) Comparison of the log-transformed ocular amyloid total surface volume between the AD ($n = 6$) group and the control group ($n = 7$). (**B**) Comparison of the brain amyloid total surface volume between the AD ($n = 10$) group and the control group ($n = 7$).

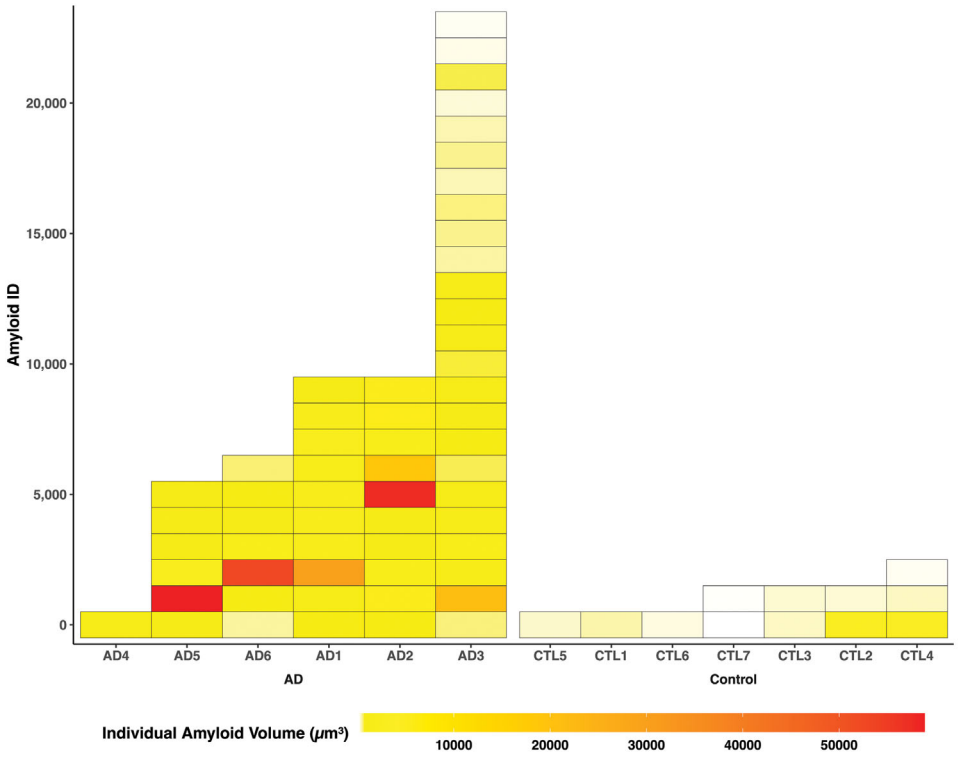

Figure 4. Visualization of intra- and inter-individual variability in amyloid particle count and volume distribution in eyeballs. Visualization of intraindividual variability in the surface volume of each amyloid particle throughout the entire eyeball architecture within the same specimen and interindividual variability concerning both the total plaque number and the individual plaque volume distribution among different specimens within the same disease group (total $n = 13$, AD = 6, control = 7). The x-axis corresponds to distinct mouse IDs in both the AD and control groups. The y-axis indicates the unique IDs of individual amyloid particles within each mouse's eyeball, whereas the z-axis quantifies the volume of individual amyloid particles (μm^3).

Investigative Ophthalmology & Visual Science

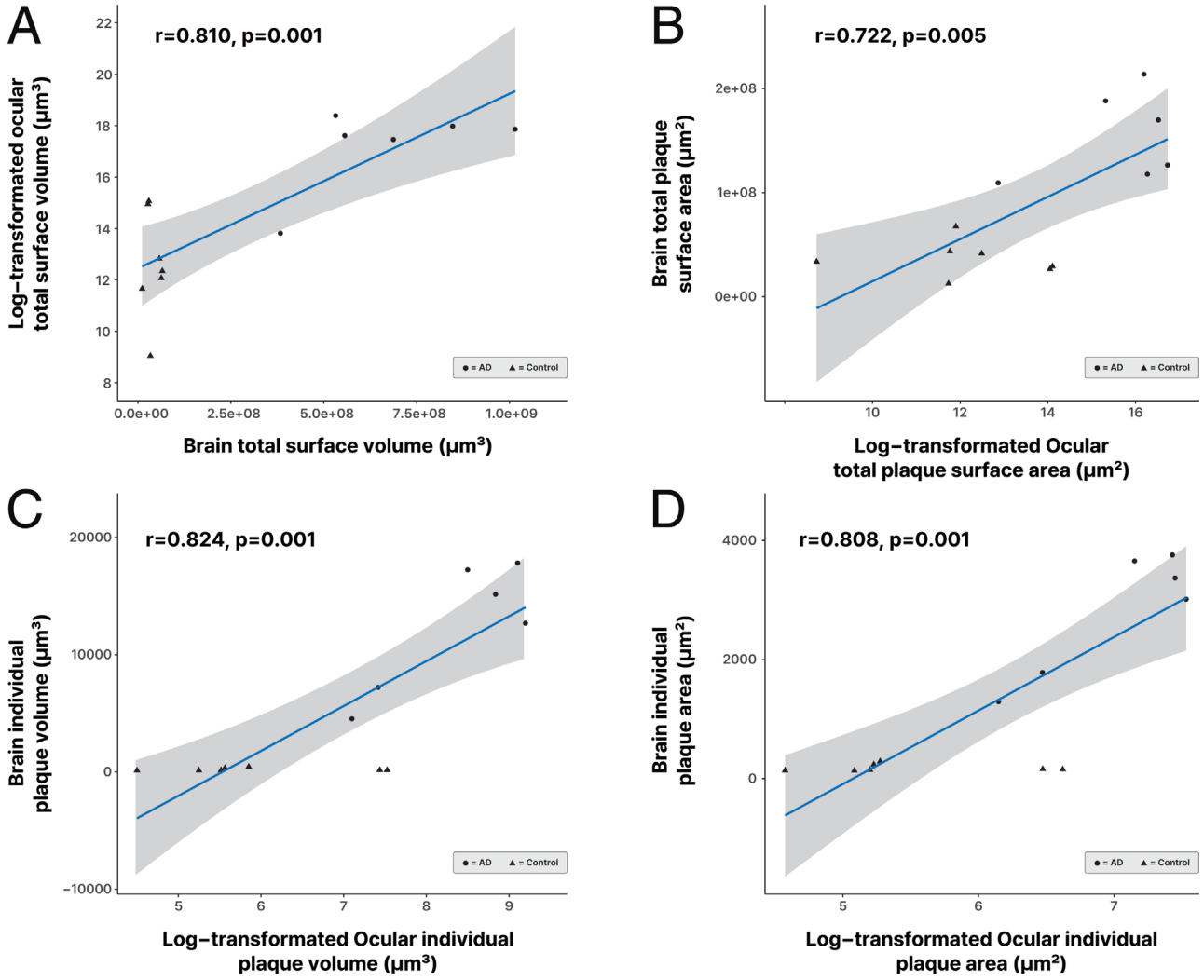

Figure 5. Correlation between quantitative and morphologic parameters of amyloid accumulation in the brain and eyeball. (**A**) Correlation between the log-transformed total surface volume (µm^3) of ocular β-amyloid and the total surface volume (µm^3) of brain β-amyloid ($r = 0.810$, $P = 0.001$) (total $n = 13$, AD = 6, control = 7). (**B**) Correlation between the log-transformed total surface area (µm^2) of ocular β-amyloid and the total surface area (µm^2) of brain β-amyloid ($r = 0.722$, $P = 0.005$). (**C**) Correlation between the log-transformed surface volume (µm^3) of individual ocular β-amyloid particle and the surface volume (µm^3) of individual brain β-amyloid particle ($r = 0.824$, $P = 0.001$). (**D**) Correlation between the log-transformed surface area (µm^2) of individual ocular β-amyloid particle and the surface area (µm^2) of individual brain β-amyloid particle ($r = 0.808$, $P = 0.001$).

Table 2. Correlation Between Quantitative and Morphologic Parameters of Amyloid Accumulation in the Brain and Eyeball

Parameter	Parameter	*n*	*r*	*P* Value*
Ocular amyloid total surface volume (µm^3)†	Brain amyloid total surface volume (µm^3)	13	0.810‡	0.001*
Ocular amyloid total plaque surface area (µm^2)†	Brain amyloid total plaque surface area (µm^2)	13	0.722‡	0.005*
Ocular amyloid individual plaque area (µm^2)†	Brain amyloid individual plaque area (µm^2)	13	0.808§	0.001*
Ocular amyloid individual plaque volume (µm^3)†	Brain amyloid individual plaque volume (µm^3)	13	0.824§	0.001*
Ocular amyloid total surface volume (µm^3)†	Amyloid PET SUVR	13	0.399‡	0.199
Ocular ellipticity (oblate)	Brain ellipticity (oblate)	13	0.420§	0.153
Ocular ellipticity (prolate)	Brain ellipticity (prolate)	13	0.531§	0.062
Ocular sphericity	Brain sphericity	13	−0.061§	0.844

* $P < 0.05$ was considered statistically significant.
† The right-skewed variables were analyzed after log transformation.
‡ Pearson correlation coefficients.
§ Spearman rank correlation coefficients.

However, no astrocyte or microglial expression of these proteins was detected in the AD eyeballs (Supplementary Fig. S2).

Discussion

Using LSFM and brain amyloid PET/MR, we conducted a comprehensive 3D spatial visualization of AD-associated neuropathology in transparent, intact 5xFAD mouse eyeballs and brains. AD mice exhibited greater accumulation of Aβ plaque-like features in both the brain and eyeball, with notable distribution not only in the retina and optic nerve but also in the more externally accessible anterior regions, including the iris, limbus, and lens, in contrast to previous studies[5–7] focusing on the retina. Furthermore, we observed a strong positive correlation between the accumulation of Aβ plaque-like features in the brain and the eyeball.

Research on AD ocular biomarkers spans three major areas: (1) retinal structural changes (e.g., retinal nerve fiber layer [RNFL] and ganglion cell–inner plexiform layer thinning), (2) Aβ/tau proteinopathies, and (3) vascular alterations.[25] Among these, early detection of ocular Aβ and tau is crucial for developing a sensitive, cost-effective biomarker for screening Aβ/tau-positive, asymptomatic individuals at risk of AD. In the mouse retina, Aβ is detected in the inner and outer nuclear layer, inner plexiform layer, and ganglion cell layer, whereas APP spans the ganglion cell layer to inner nuclear layers.[26] In previous investigations of the physiologic roles of Aβ and APP in the normal visual functions,[27] APP is essential for retinal synaptogenesis, glial differentiation, angiogenesis, and neuronal survival in rodents.[28,29] Genetic and AD risk factors, such as apolipoprotein E and iron overload, can disrupt retinal APP processing, leading to Aβ plaque overproduction.[30] Aβ has been detected in both mouse and human retinas, although inconsistencies across studies may reflect differences in species, age, sex, genetics, disease severity, sample size, or staining methods. Williams et al.[31] found no evidence of tau, Aβ, TDP-43, ubiquitin, or α-synuclein in the eyes of 17 patients with AD, regardless of disease severity. In contrast, a postmortem cohort from the Netherlands Brain Bank identified Aβ-positive structures in the human retina, including aggregates in vessel walls, globular deposits in the photoreceptor layer, and cytoplasmic granular deposits in ganglion cells.[32] While the co-occurrence of pathological proteins observed in the brain is only partially reflected in the retina, these findings nonetheless support the presence of hallmark neurodegenerative disease proteins in retinal tissue.[32] Histologic studies of postmortem human eyes have identified neuritic plaques in the retinas of patients with AD using Gallyas silver and 6E10 antibody staining.[33,34] Similarly, Moncaster et al.[8] demonstrated Aβ pathology in the lenses of both patients with AD and Tg2576 transgenic mice, highlighting its potential as an accessible biomarker for early detection and monitoring of AD. Supporting this, fluorescent ligand eye scanning successfully distinguished patients with AD from healthy individuals with 85% sensitivity and 95% specificity by detecting exogenous ligands bound to lens Aβ.[35] Koronyo-Hamaoui et al.[5] identified retinal Aβ with high diagnostic accuracy in postmortem samples from patients with AD (sensitivity = 1.00, specificity = 1.00, diagnostic odds ratio $\geq$ 187.00). In vivo imaging of transgenic APPSWE/PS1ΔE9 mice treated with curcumin and Aβ antibody clones further suggested that retinal Aβ plaque formation precedes brain deposition.[5] Sampani et al.[36] reported higher concentrations of AD biomarkers in ocular fluids compared to plasma, with significant correlations between the two compartments.

Our study is the first to demonstrate that total plaque-like feature load, measured three-dimensionally by total surface volume across the entire eyeball, shows a strong positive correlation ($r = 0.810$, $P = 0.001$) with the whole-brain plaque-like feature load—a relationship that previous studies could not adequately assess due to limitations in measurement techniques. We also observed a strong correlation between the individual surface area and volume of plaque-like features in the eyeball and brain. In the meta-analysis, the limited number of eligible studies has hindered a clear elucidation of the interaction between retinal Aβ and brain Aβ.[37] Although Koronyo-Hamaoui et al.[5] assessed Aβ in both the brain and the retina, their evaluation was limited to qualitative visual detection of the concurrent presence of Aβ in both tissues without providing quantitative correlation data on Aβ levels. Their 2D cross-sectional analysis of retinal flat mounts measured plaque count and area but excluded certain amyloid particles due to sectioning angles and lacked the ability to differentiate between a few large plaques and numerous smaller ones, limiting the precision of total amyloid burden assessments. Using Imaris-based 3D surface models,[38] we quantified the total surface volume of plaque-like features within the intact spherical ocular structure by summing the 3D-rendered individual volumes, providing a more accurate representation of amyloid load. We selected total surface volume as the representative measure of ocular plaque-like features, as volumetric assessments provide a more comprehensive reflection of the true pathological burden compared to particle counts alone.[39]

Although complex 3D amyloid patterns (TAPs, three-dimensional amyloid patterns) have been identified in human AD brain tissue,[40] no prior studies have investigated the morphologic correlation between plaque-like features in the brain and eye. In our study, we found no significant correlation between these morphologic parameters, indicating that plaque-like features in the eye may differ morphologically from those in the brain. By assigning unique identifiers to each individual plaque-like feature, we not only quantified the total plaque-like feature load in the entire eyeball but also measured 3D morphologic features, such as ellipticity and sphericity. Our analysis demonstrated significant intraindividual variability in the surface volumes of plaque-like features within the same specimen and interindividual differences in the number and volume distribution among different AD mice. For example, mouse 1 exhibited a total surface volume of 44,786,904 μm^3, with fewer but larger plaque-like features (average volume: 4915 μm^3; total particle number: 9113), while mouse 3 had a total surface volume of 38,488,272 μm^3 but a greater number of smaller particles (average volume: 1663 μm^3; total particle number: 23,143). Previous investigations into the structure–toxicity relationship of A$\beta_{1\text{-}42}$ aggregates suggested a correlation between various conformational entities of Aβ and neurotoxicity in AD.[41] Although they share an identical amino acid sequence, more regular and longer Aβ fibrils exhibit intrinsic toxicity.[41]

Although our findings do not definitively identify whether the total number, volume, size, or shape of plaque-like features holds the greatest prognostic value, they may provide valuable insights into the relationship between 3D amyloid morphology and the treatment outcome of more effective structure-based AD therapies in future studies.

Investigative Ophthalmology & Visual Science

Our visual analysis of [^{18}F]Flutemetamol brain PET/MRI showed greater amyloid uptake in AD mice compared to controls, although cortical SUVR differences were not statistically significant. Ocular uptake in PET imaging was likely due to nonspecific radiopharmaceutical binding, which interfered with the accuracy of measurements, making quantitative analysis in the eyeball infeasible. This nonspecific uptake can occur when radiopharmaceuticals bind to nontarget tissues or are distributed unexpectedly within the body, complicating data interpretation.[42] Although amyloid PET imaging is crucial in clinical settings for noninvasive early AD detection, quantifying amyloid PET imaging in preclinical mouse studies presents several challenges. The lower spatial resolution of small-animal PET complicates the precise measurement of plaque location and quantity, limiting accurate tracking in specific brain regions. Additionally, nonspecific binding in PET imaging complicates accurate amyloid burden quantification, causing discrepancies between preclinical mouse data and clinical findings.[43] Addressing these limitations is crucial for improving the translational relevance of amyloid PET imaging in preclinical studies and enhancing the evaluation of potential AD treatments. We believe that the 3D analytical method tested in this study can provide meaningful information in preclinical settings, offering great potential as a robust tool for efficacy evaluation in future drug development.

Although neuroinflammation was not observed in our eyeball samples, previous reports have documented its presence in the eyes of patients with AD. Glial fibrillary acidic protein (GFAP) immunoreactivity is elevated in the retinal ganglion cell layer in patients with AD.[44] Given that early-stage neuroinflammation precedes later-stage neurodegeneration,[45,46] the absence of astrocytes and microglia in our AD eyeball samples might reflect early neuroinflammation not detectable in 44-week-old AD mouse eyeballs. Alternatively, it could be due to limitations in antibody efficacy, including poor penetration or nonspecific surface labeling.

Regarding study limitation, our data provide a cross-sectional snapshot of ocular and brain Aβ pathology in 44-week-old 5xFAD mice, lacking a longitudinal perspective on disease progression over the life span. An umbrella review of 14 meta-analyses underscored the limitations of cross-sectional designs, showing poor to moderate accuracy in detecting AD through OCT metrics such as RNFL thickness and prosaccade latency in a cross-sectional setting.[47] Future well-designed longitudinal studies are necessary to track ocular Aβ pathology over the life span, from the very early stages to severe AD, and determine if these changes could better predict AD onset. Additionally, future research should comprehensively assess relationships among ocular and brain pathology, evaluate visual and cognitive function, and perform intraregional correlation analyses between brain and eye subregions. Furthermore, discrepancies between LSFM and PET imaging outcomes may partly reflect an overestimation of amyloid pathology by LSFM. Thioflavin-S staining, widely used to detect Aβ plaque-like features, has limitations due to its nonspecific binding to other β-sheet–rich structures, such as p-tau aggregates, necessitating caution when using thioflavin-S as an Aβ-detecting probe in 5xFAD mice. Despite these challenges, thioflavin-S was chosen over anti-Aβ antibodies in this study due to the challenges of antibody penetration in thick, whole-organ samples because its small-molecule properties allow for consistent and uniform staining. However, prior studies have reported that thioflavin-S–labeled protein aggregates in the cortical and hippocampal regions of 5xFAD mice did not correspond to anti-Aβ antibody staining.[48] High dye concentrations have also been associated with nonspecific staining and red-shifted fluorescence, underscoring the need to optimize thioflavin-S protocols.[16] These findings emphasize the importance of using complementary techniques, such as Aβ antibody colabeling, ELISA, Western blotting, or mass spectrometry, to achieve a more accurate and balanced interpretation of amyloid pathology.[48] Nonetheless, we optimized the staining protocol to minimize potential overestimation. Although thioflavin-S staining result may still lead to some overestimation of the absolute Aβ burden, the use of a uniform staining protocol for both brain and ocular tissues ensures that any resulting overestimation remains proportionate, thereby preserving the strength and significance of the observed correlation.

Our novel observation of a robust positive correlation between 3D-measured Aβ plaque-like feature burden in the whole eyeball and its concurrent presence in the brain, particularly in accessible regions like the iris and lens, highlights the systemic nature of Aβ pathology. Our results raise the possibility that ocular Aβ levels could serve as independent predictors of brain Aβ burden. Given the routine nature of ophthalmologic exams for adults older than 50 years, incorporating ocular Aβ biomarkers into primary care may offer a practical and accessible alternative to advanced neuroimaging, particularly in resource-limited settings, and could potentially aid in identifying candidates for early preventive AD interventions.

Acknowledgments

The authors thank the PET core of the Convergence Medicine Research Center at the Asan Institute for Life Sciences, Asan Medical Center (Director: Prof. Jae Seung Kim) for their assistance with [^{18}F]Flutemetamol brain PET/MR imaging. They also thank the MRI core of the Convergence Medicine Research Center for their support in acquiring 7T brain MRI images for amyloid PET template creation and Seonghyun Kim for his valuable contributions to animal care, tissue clearing, and immunostain.

Supported by the research fund of Dankook University in 2025.

Disclosure: **H.J. Son**, None; **S. Kim**, None; **S.-Y. Kim**, None; **J.H. Jung**, None; **S.H. Lee**, None; **S.-J. Kim**, None; **C. Kim**, None; **A. Hahn**, None

References

1. Park KW. Anti-amyloid antibody therapies for Alzheimer's disease. *Nucl Med Mol Imaging*. 2024;58:227–236.
2. Van Dyck CH, Swanson CJ, Aisen P, et al. Lecanemab in early Alzheimer's disease. *N Engl J Med*. 2023;388:9–21.
3. London A, Benhar I, Schwartz M. The retina as a window to the brain-from eye research to CNS disorders. *Nat Rev Neurol*. 2013;9:44–53.
4. Sadun AA, Bassi CJ. Optic nerve damage in Alzheimer's disease. *Ophthalmology*. 1990;97:9–17.
5. Koronyo-Hamaoui M, Koronyo Y, Ljubimov AV, et al. Identification of amyloid plaques in retinas from Alzheimer's patients and noninvasive in vivo optical imaging of retinal plaques in a mouse model. *Neuroimage*. 2011;54:S204–S217.

6. La Morgia C, Ross-Cisneros FN, Koronyo Y, et al. Melanopsin retinal ganglion cell loss in Alzheimer disease. *Ann Neurol*. 2016;79:90–109.
7. Ning A, Cui J, To E, Ashe KH, Matsubara J. Amyloid-β deposits lead to retinal degeneration in a mouse model of Alzheimer disease. *Invest Ophthalmol Vis Sci*. 2008;49:5136–5143.
8. Moncaster JA, Moir RD, Burton MA, et al. Alzheimer's disease amyloid-β pathology in the lens of the eye. *Exp Eye Res*. 2022;221:108974.
9. Mei X, Yang M, Zhu L, et al. Retinal levels of amyloid beta correlate with cerebral levels of amyloid beta in young APPswe/PS1dE9 transgenic mice before onset of Alzheimer's disease. *Behav Neurol*. 2020;2020:1574816.
10. Huisken J, Swoger J, Del Bene F, Wittbrodt J, Stelzer EH. Optical sectioning deep inside live embryos by selective plane illumination microscopy. *Science*. 2004;305:1007–1009.
11. Oakley H, Cole SL, Logan S, et al. Intraneuronal β-amyloid aggregates, neurodegeneration, and neuron loss in transgenic mice with five familial Alzheimer's disease mutations: potential factors in amyloid plaque formation. *J Neurosci*. 2006;26:10129–10140.
12. Habiba U, Merlin S, Lim JKH, et al. Age-specific retinal and cerebral immunodetection of amyloid-β plaques and oligomers in a rodent model of Alzheimer's disease. *J Alzheimers Dis*. 2020;76:1135–1150.
13. Lim JKH, Li QX, He Z, et al. Retinal functional and structural changes in the 5xFAD mouse model of Alzheimer's disease. *Front Neurosci*. 2020;14:862.
14. Mirrione MM, Schiffer WK, Fowler JS, Alexoff DL, Dewey SL, Tsirka SE. A novel approach for imaging brain-behavior relationships in mice reveals unexpected metabolic patterns during seizures in the absence of tissue plasminogen activator. *Neuroimage*. 2007;38:34–42.
15. Ma Y, Hof PR, Grant SC, et al. A three-dimensional digital atlas database of the adult C57BL/6J mouse brain by magnetic resonance microscopy. *Neuroscience*. 2005;135:1203–1215.
16. MacKeigan TP, Morgan ML, Stys PK. Quantitation of tissue amyloid via fluorescence spectroscopy using controlled concentrations of thioflavin-S. *Molecules*. 2023;28(11):4483.
17. Ridler TW, Calvard S. Picture thresholding using an iterative selection method. *IEEE Trans Syst Man Cybern*. 1978;8:630–632.
18. Bitplane. *Imaris Reference Manual*. Concord, MA: Bitplane; 2017.
19. Oberholzer M, Ostreicher M, Christen H, Brühlmann M. Methods in quantitative image analysis. *Histochem Cell Biol*. 1996;105:333–355.
20. Pham DL, Xu C, Prince JL. Current methods in medical image segmentation. *Annu Rev Biomed Eng*. 2000;2:315–337.
21. Otsu N. A threshold selection method from gray-level histograms. *Automatica*. 1975;11:23–27.
22. Niblack W. *An Introduction to Digital Image Processing*. New York, NY: Strandberg Publishing Company; 1985.
23. Stockman G, Shapiro LG. *Computer Vision*. Upper Saddle River, NJ: Prentice Hall PTR; 2001.
24. Chaubey AK. Comparison of the local and global thresholding methods in image segmentation. *World J Res Rev*. 2016;2:1–4.
25. Alber J, Goldfarb D, Thompson LI, et al. Developing retinal biomarkers for the earliest stages of Alzheimer's disease: what we know, what we don't, and how to move forward. *Alzheimers Dement*. 2020;16:229–243.
26. Javaid FZ, Brenton J, Guo L, Cordeiro MF. Visual and ocular manifestations of Alzheimer's disease and their use as biomarkers for diagnosis and progression. *Front Neurol*. 2016;7:55.
27. Hernández-Zimbrón LF, Perez-Hernández M, Torres-Romero A, et al. Markers of Alzheimer's disease in primary visual cortex in normal aging in mice. *Biomed Res Int*. 2017;2017:3706018.
28. Chen ST, Patel AJ, Garey LJ, Jen LS. Expression of βb-amyloid precursor protein immunoreactivity in the retina of the rat during normal development and after neonatal optic tract lesion. *Neuroreport*. 1997;8:713–717.
29. Ho T, Vessey KA, Cappai R, et al. Amyloid precursor protein is required for normal function of the rod and cone pathways in the mouse retina. *PLoS One*. 2012;7:e29892.
30. Shah T, Gupta S, Chatterjee P, Campbell M, Martins R. Beta-amyloid sequelae in the eye: a critical review on its diagnostic significance and clinical relevance in Alzheimer's disease. *Mol Psychiatry*. 2017;22:353–363.
31. Williams EA, McGuone D, Frosch MP, Hyman BT, Laver N, Stemmer-Rachamimov A. Absence of Alzheimer disease neuropathologic changes in eyes of subjects with Alzheimer disease. *J Neuropathol Exp Neurol*. 2017;76:376–383.
32. Hart de Ruyter FJ, Evers M, Morrema THJ, et al. Neuropathological hallmarks in the post-mortem retina of neurodegenerative diseases. *Acta Neuropathol*. 2024;148:24.
33. Koronyo Y, Biggs D, Barron E, et al. Retinal amyloid pathology and proof-of-concept imaging trial in Alzheimer's disease. *JCI Insight*. 2017;2(16):e93717.
34. Tsai Y, Lu B, Ljubimov AV, et al. Ocular changes in TgF344-AD rat model of Alzheimer's disease. *Invest Ophthalmol Vis Sci*. 2014;55:523–534.
35. Kerbage C, Sadowsky CH, Tariot PN, et al. Detection of amyloid β signature in the lens and its correlation in the brain to aid in the diagnosis of Alzheimer's disease. *Am J Alzheimers Dis Other Demen*. 2015;30:738–745.
36. Sampani K, Ness S, Tuz-Zahra F, et al. Neurodegenerative biomarkers in different chambers of the eye relative to plasma: an agreement validation study. *Alzheimers Res Ther*. 2024;16:192.
37. Jiang J, Wang H, Li W, Cao X, Li C. Amyloid plaques in retina for diagnosis in Alzheimer's patients: a meta-analysis. *Front Aging Neurosci*. 2016;8:267.
38. Crassin C. *GigaVoxels: A Voxel-Based Rendering Pipeline for Efficient Exploration of Large and Detailed Scenes*. Grenoble, France: Université de Grenoble; 2011.
39. Demir I, Westermann R. *Vector-to-Closest-Point Octree for Surface Ray-Casting*. Nicosia, Cyprus: The Eurographics Association; 2015.
40. Liebmann T, Renier N, Bettayeb K, Greengard P, Tessier-Lavigne M, Flajolet M. Three-dimensional study of Alzheimer's disease hallmarks using the iDISCO clearing method. *Cell Rep*. 2016;16:1138–1152.
41. Lührs T, Ritter C, Adrian M, et al. 3D structure of Alzheimer's amyloid-$\beta_{1\text{-}42}$ fibrils. *Proc Natl Acad Sci USA*. 2005;102:17342–17347.
42. Kristensen LK, Christensen C, Jensen MM, et al. Site-specifically labeled (89)Zr-DFO-trastuzumab improves immuno-reactivity and tumor uptake for immuno-PET in a subcutaneous HER2-positive xenograft mouse model. *Theranostics*. 2019;9:4409–4420.
43. Frost GR, Longo V, Li T, et al. Hybrid PET/MRI enables high-spatial resolution, quantitative imaging of amyloid plaques in an Alzheimer's disease mouse model. *Sci Rep*. 2020;10:10379.

Investigative Ophthalmology & Visual Science

44. Blanks JC, Schmidt SY, Torigoe Y, Porrello KV, Hinton DR, Blanks RH. Retinal pathology in Alzheimer's disease. II. Regional neuron loss and glial changes in GCL. *Neurobiol Aging*. 1996;17:385–395.
45. Lee N, Choi JY, Ryu YH. The development status of PET radiotracers for evaluating neuroinflammation. *Nucl Med Mol Imaging*. 2024;58:160–176.
46. Nam MH, Na H, Justin Lee C, Yun M. A key mediator and imaging target in Alzheimer's disease: unlocking the role of reactive astrogliosis through MAOB. *Nucl Med Mol Imaging*. 2024;58:177–184.
47. Costanzo E, Lengyel I, Parravano M, et al. Ocular biomarkers for Alzheimer disease dementia: an umbrella review of systematic reviews and meta-analyses. *JAMA Ophthalmol*. 2023;141:84–91.
48. Shin J, Park S, Lee H, Kim Y. Thioflavin-positive tau aggregates complicating quantification of amyloid plaques in the brain of 5XFAD transgenic mouse model. *Sci Rep*. 2021;11:1617.

Supplementary Material

Supplementary Video S1. Representative light-sheet fluorescence microscope image of β-amyloid in the eyeballs of 5xFAD mice. Representative image of light-sheet fluorescence microscope imaging with hydrophilic tissue clearing and volume staining using thioflavin-S (488 nm, green channel) for β-amyloid in the eyeballs of 5xFAD mice.

Supplementary Video S2. Representative light-sheet fluorescence microscope image of β-amyloid in the eyeballs of control mice. Representative image of light-sheet fluorescence microscope imaging with hydrophilic tissue clearing and volume staining using thioflavin-S (488 nm, green channel) for β-amyloid in the eyeballs of control mice.

Supplementary Video S3. Representative light-sheet fluorescence microscope images of β-amyloid, astrocyte, and microglia in the brains of 5xFAD mice. Representative images of light-sheet fluorescence microscope imaging with hydrophilic tissue clearing and volume immunostaining of the brains of 44-week-old 5xFAD mice. Green channel (488 nm) with volume staining with thioflavin-S, a specific marker for amyloid. Purple channel (647 nm) with volume immunostaining with anti–ACSA-2, a specific marker for astrocytes. Red channel (561 nm) with volume immunostaining with anti-CD11b, a specific marker for microglia.

Supplementary Video S4. Interindividual variability concerning the number and surface volume of each individual amyloid particle throughout the entire eyeball architecture among mice (total n = 13, AD = 6, control = 7). The x-axis corresponds to distinct mouse IDs in both the AD and control groups. The y-axis indicates the unique IDs of individual amyloid particles within each mouse's eyeball, whereas the z-axis quantifies the volumes of individual amyloid particles (μm^3).

Investigative Ophthalmology & Visual Science